# Properties of polycapillary optics dedicated to low-energy parallel-beam wavelength-dispersive spectrometers for synchrotron-based X-ray fluorescence study

P. Jagodzinski, M. Pajek, D. Banas, A. Kubala-Kukus, J. Szlachetko, M. Cotte, M. Salome

Research Article | Vol. 29, No. 17 / 16 Aug 2021 / Optics Express 27193
Optics EXPRESS

# Properties of polycapillary optics dedicated to low-energy parallel-beam wavelength-dispersive spectrometers for synchrotron-based X-ray fluorescence study

P. JAGODZIŃSKI,[1,*] M. PAJEK,[1] D. BANAŚ,[1] A. KUBALA-KUKUŚ,[1] J. SZLACHETKO,[2] M. COTTE,[3,4] AND M. SALOMÉ[3]

[1]*Institute of Physics, Jan Kochanowski University, PL-25-406 Kielce, Poland*
[2]*Institute of Nuclear Physics Polish Academy of Science, PL-31-342 Kraków, Poland*
[3]*European Synchrotron Radiation Facility, F-38000 Grenoble Cedex 9, France*
[4]*Sorbonne Université, CNRS, Laboratoire d'Archéologie Moléculaire et Structurale, LAMS, F- 75005 Paris, France*
[*]*pawel.jagodzinski@ujk.edu.pl*

**Abstract:** The main advantage of wavelength-dispersive spectrometers applied in X-ray study is their high energy resolution. The design and construction of spectrometer, usually dedicated to the specific experimental systems, for example synchrotron based setups, need information about the characteristics of the main elements of the spectrometer such as X-ray optics elements, crystals and detectors. Such information can be obtained using Monte-Carlo simulations. In this paper, the Monte-Carlo simulations of X-ray tracing in parallel-beam wavelength-dispersive spectrometer (PBWDS), equipped with polycapillary optics, are presented and discussed. The study concentrates on the description of the polycapillary model, simulations of the properties of X-ray polycapillary optics and, finally, on the simulations of X-ray track in the spectrometer designed and installed at the ID21 beamline at the European Synchrotron Radiation Facility (ESRF, Grenoble, France). The results of simulations were compared with experimental data obtained for different registered X-ray energies and spectrometer crystals, showing good agreement. The obtained results showed that the X-ray transmission in the tested polycapillary optics is at the level of 15%, while the divergence of the outgoing beam changes from 8 mrad to 3 mrad with an increase of photon energy from 2 keV to 10 keV. The spectrometer provides an energy resolution of 5 eV and 33 eV in the energy range of 1.4 keV - 6.5 keV. The developed simulation program can be successfully used for the construction of spectrometers dedicated to the different experimental conditions.



## 1. Introduction

The study of the X-ray fluorescence radiation emitted by medium is the basis of many X-ray spectrometry techniques dedicated for elemental analysis and widely used in such different fields as materials science, geology, biology or medicine [1–3]. The difficulty of the X-ray fluorescence studies is the fact that the radiation is usually emitted from the studied sample by atoms of many elements and in registered spectra the X-ray emission lines overlapping can be observed. This is especially probable when energy dispersive spectrometers (EDS), with energy resolution of over one hundred of electron volts [4], are applied for measurements. For better separation of emission lines, the wavelength-dispersive spectrometers can be applied [5–7]. This type of device, i.e. compact parallel-beam wavelength-dispersive spectrometer (PBWDS), based on flat crystal and polycapillary optics [8–12] was designed and installed at the ID21 beamline at the European Synchrotron Radiation Facility (ESRF), (described earlier in details by Szlachetko *et al* [13]). The PBWDS spectrometer has been used in applied research, i.a., to study of trace elements

#424530 https://doi.org/10.1364/OE.424530
Journal © 2021 Received 17 Mar 2021; revised 16 Jul 2021; accepted 17 Jul 2021; published 9 Aug 2021

Optics EXPRESS

contents in archaeological materials [4,14] with energy resolution at the level of single eV. The high energy resolution of this spectrometer allowed also for the first observation of the correlated two-electron one-photon transitions in single-photon $K$-shell double ionization [15].

The principle of operation of the wavelength-dispersive spectrometers is based on the wave nature of the X-rays. According to the Braggs law [16], only photons with wavelength fulfilling this law are diffracted from crystal planes. The energy selection can be done by rotating the crystals, which is accompanied by an angular deviation of the diffracted beam. The phenomena of diffraction on the crystal is used to spread out the incident radiation with different wavelengths. The wavelength-dispersive spectrometers can operate in various geometries. The geometry with flat crystal is characterized by very simple construction, but also by low efficiency. However, the low efficiency can be improved by forming the parallel incoming beam directed on the crystal, which can be obtained by polycapillary optics system ( Fig. 1). Polycapillary optics is a widely used technology for collimating and guiding X-ray beams. The development of the polycapillary optics has become an active direction for X-ray research due to its wide potential applications in many fields, such as high-quality X-ray diffraction [17], chemical mapping [18], collection of astronomical signals optics [19] or a variety of clinical applications: mammography, protein crystallography [20], choroidal melanoma and iris melanoma [21], as well as might create novel instruments and methods for future applied techniques [22].

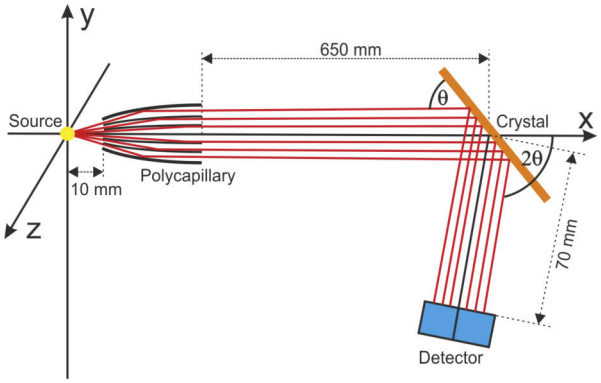


**Fig. 1.** Geometry of PBWDS spectrometer used in the simulations. The $\theta$-$2\theta$ rotation allows for Bragg angles between 20° and 70°.

This paper is an extension of our previous work [13], and is focused on the detailed Monte-Carlo X-ray-tracing study of propagation of X-rays through the polycapillary optics affecting the exit divergence, spatial distribution of X-rays after passing through this optic element, and as a consequence, on the energy resolution of the PBWDS spectrometer.

## 2. Monte-Carlo X-ray-tracing simulation

The geometry of the low-energy parallel-beam wavelength-dispersive spectrometer discussed in this paper is presented in Fig. 1. The main elements of this geometry are: polycapillary for tracing X-ray emitted from the sample (source), crystal and detector. A straightforward procedure to determine the characteristics of a polycapillary optics as well as to better understand the optical properties of a parallel-beam wavelength-dispersive spectrometer is a X-ray-tracing simulation approach. The Monte-Carlo method is especially well suited and efficient in cases, for which, due to the complexity of the problem, a fully analytical treatment is impractical. In the case of use a polycapillary optics, the X-ray-tracing allows a detailed investigation of X-rays propagation process through a polycapillary fibers, and predicts the transmission, the beam divergence at the output, if only the parameters such as: polycapillary length, focal distance, entrance and

Optics EXPRESS

exit sizes, single fiber diameter and wall thickness, are known. The Monte-Carlo X-ray-tracing program [23,24] discussed in this paper allows to study mentioned characteristics and also to predict the intensity distribution of X-rays on a detector and to determine the energy resolution of the PBWDS spectrometer. This computer program is written in C++. In the program the random number generator based on an Mersenne Twister algorithm [25] was used to generate numbers with uniform distributions, which were then transformed to the random numbers having assumed distributions. The program tracks the trajectory of each photon emitted randomly from the X-ray source (sample) and tests whether this photon is transmitted through the polycapillary, next diffracted by the crystal and finally registered by the detector. In the case that the photon reaches the polycapillary, the total external reflection condition [26,27] is considered. The photon transmitted through the polycapillary is then traced to the crystal, and in the case it reaches its surface, the diffraction process, described by the crystal rocking curve (from XOP2.3 [28,29]) and dynamical theory of diffraction [5,6], is considered. The photon diffracted by the crystal is next traced on its way to the 2D-detector.

The presentation of the Monte-Carlo X-ray-tracing simulation starts from polycapillary model description. Next, the simulation of X-ray polycapillary optics properties are presented and, finally, the simulations of X-ray track in the spectrometer.

### 2.1. Polycapillary model

The rapid development of the X-ray polycapillary optics caused the increasing demand for a simulation tool that takes into account real physical properties of the polycapillaries (such as surface roughness), as well as correctly describing the real shape resulting from the production process. There are a few models and several codes to calculate X-ray transmission by mono- or poly- capillary. Some of them describe only single fiber [30–32], others describe capillaries in a specific configuration, e.g. for focusing beam [30,33–38] or show the results for hard X-rays energy [39,40]. The most advanced codes for ray-tracing of X-ray inside fibers channel [30,41–43], namely GXPS [44], SHADOW [35,37,45–47], PolyCAD [48,49], include absorption corrections and polycapillary roughness.

The polycapillary optics (*full-lens* or *half-lens*) elements are produced by heating bundles of parallel tubes, pulling them to a specified shape and cutting [9,50–52]. The half-lens can work in focusing or collimating geometries by bending the fibers to an appropriate curvature. In order to obtain the quasi-parallel X-ray beam at the exit of the polycapillary, the condition of parallelism of fibers at the end of polycapillary has to be fullfiled [9,49]. On the other hand to focus the nearly parallel X-rays beam at the exit of the polycapillary, the fibers on entrance of the polycapillary must be parallel [9,49]. Most of the available simulation codes can be used to calculate capillary properties only for simple shapes of fiber, like cylindrical, conical, or ellipsoidal. They cannot simulate the polycapillaries with polynomial profiles higher than binomial. These shapes do not describe properly the polycapillary dedicated for collimating the quasi-parallel X-ray beam. In order to meet boundary condition of fibers parallelism, the third-degree polynomial function, describing the shape of single fiber curvature, was applied in our simulation program.

The polycapillary consists of thousands of fibers curved and arranged in hexagonal bunch (see Fig. 2(a)). The X-rays hitting the internal surface of the fibers at the angle, less than the critical angle $\theta_{crit}$ (measured between surface and X-ray direction) of total external reflection (see Refs. [26,27]), propagate along this fiber by multiple reflections. This reflection process occurs because the refractive index of the polycapillary material for X-rays is less than unity. Generally, the properties of the X-rays beam transmitted through the polycapillary depend on the energy of the X-rays, the source size, the shape and the size of the polycapillary as well as on the polycapillary material and its surface roughness.

In our application the most important aspect was to develop the simulation software to predict properties of parallel-beam wavelength-dispersive crystal spectrometer equipped with

Optics EXPRESS

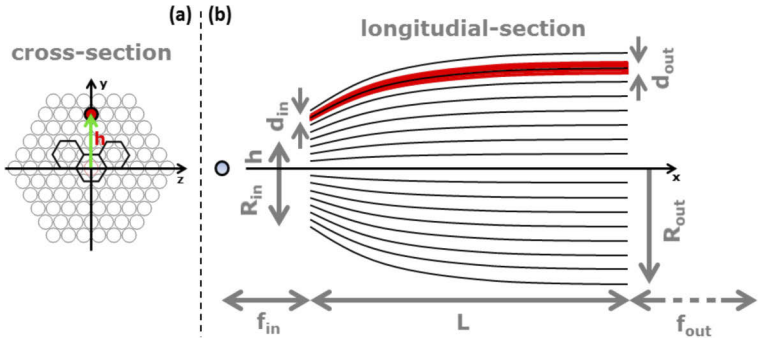


**Fig. 2.** (a) Polycapillary cross-section. (b) Scheme of the glass polycapillary showing its main characteristics: length $L$, entrance radius $R_{in}$, exit radius $R_{out}$, distance of fiber entrance to the polycapillary axis of symmetry $h$, entrance focal distances $f_{in}$, exit focal distance $f_{out}$, single fiber inner entrance diameter $d_{in}$ and inner exit diameter $d_{out}$. The single fiber is marked in red.

polycapillary optics, based only on the geometrical parameters of polycapillary provided together with the polycapillary by manufacturer, such as length, focal distance, entrance and exit sizes. Others necessary parameters such as single fiber diameter and wall thickness were taken from the publication of the manufacturer for typical $SiO_2$ polycapillary (see Schields *et al* [12]).

In the applied X-ray-tracing method, the path of each photon randomly emitted from the X-ray source, is followed in a polycapillary fiber taking into account its reflection and refraction (i.e. absorption) in the case of hitting the inner side of the fiber wall. The reflection coefficient of a photon from a smooth surface can be calculated from the Fresnel equations [26]. In particular, X-rays for small angles of incidence, being below the critical angle $\theta_{crit}$, are practically totally reflected. The phenomenon of total external reflection of X-rays is described in details in Refs. [26,27]. For realistic glass polycapillaries, the surface is not ideally smooth and consequently, the corrections describing the surface roughness have to be considered. In the present paper the surface roughness effects were treated using two models: the exponential damping factor approach [30] and Kimball [53] theory.

In the present study the polycapillary cross-section is described as a bundle of thin, closely packed, circular fibers arranged in a hexagonal pattern (see Fig. 2(a)). Dimensions of polycapillary are characterized by the following parameters: length $L$, radii of entrance $R_{in}$ and exit $R_{out}$, focal distances of entrance $f_{in}$ and exit $f_{out}$, single fiber inner diameters on entrance $d_{in}$ and exit $d_{out}$ (see Fig. 2(b)). In our polycapillary model the ratio of single fiber exit and entrance diameters is equal to the ratio of polycapillary exit and entrance sizes $\left(\frac{d_{out}}{d_{in}} = \frac{R_{out}}{R_{in}}\right)$. This model also takes into account the variable thickness of the fiber wall, which changed proportional to the fiber diameter. The value of the wall thickness on the fibers entrance was estimated from the SEM photo presented in [12]. Since the real polycapillary shape is not known, the geometric model described mathematically by Eqs. (1), (2), (3), (4) was assumed.

In our simulation program, the third-degree polynomial function $T(x, h)$ (Eq. (1)), describing the distance of fiber center to polycapillary $x$-axis (see Fig. 2), was applied to characterize the shape of fibers:

$$T(x, h) = C_0(h) + C_1(h)x + C_2(h)x^2 + C_3(h)x^3, \tag{1}$$

where $h$ is the distance of fiber entrance to the polycapillary axis of symmetry ($x$-axis on Fig. 2), and $C_i(h)$, where $i = 0, 1, 2, 3$, are the polynomial coefficients depending on the parameters ($L$, $R_{in}$, $R_{out}$, $f_{in}$, $f_{out}$) as well as type (collimating/focusing) of polycapillary. The case of collimating a quasi-parallel X-ray beam from a point X-ray source means, from a mathematical point of view,

Optics EXPRESS

that the exit focal distance $f_{out} \rightarrow \infty$. The $C_i(h)$ polynomial coefficients for this case conditions are described by Eq. (2):

$$\begin{cases} T(0,h) = h, \\ T(L,h) = h\dfrac{R_{out}}{R_{in}}, \\ \left.\dfrac{\partial T(x,h)}{\partial x}\right|_{x=0} = \dfrac{h}{f_{in}}, \\ \left.\dfrac{\partial T(x,h)}{\partial x}\right|_{x=L} = 0, \end{cases} \tag{2}$$

whereas the case of focusing nearly parallel photon beam is described by Eq. (3):

$$\begin{cases} T(0,h) = h, \\ T(L,h) = h\dfrac{R_{out}}{R_{in}}, \\ \left.\dfrac{\partial T(x,h)}{\partial x}\right|_{x=0} = 0, \\ \left.\dfrac{\partial T(x,h)}{\partial x}\right|_{x=L} = -\dfrac{h}{f_{out}}\dfrac{R_{out}}{R_{in}}. \end{cases} \tag{3}$$

A cross-section of single polycapillary fiber was assumed to be a circle with continuously varying radius $r(x)$ along a central axis of the polycapillary ($x$-axis) and is described by Eq. (4):

$$[y - T(x,h)\cos(\phi)]^2 + [z - T(x,h)\sin(\phi)]^2 = r^2(x), \tag{4}$$

where $\phi$ is the angle in $yz$ plane (cross-section plane).

The Fig. 3 shows the shape of few fibers used for polycapillary simulation obtained based on Eqs. (1), (2), and (4).

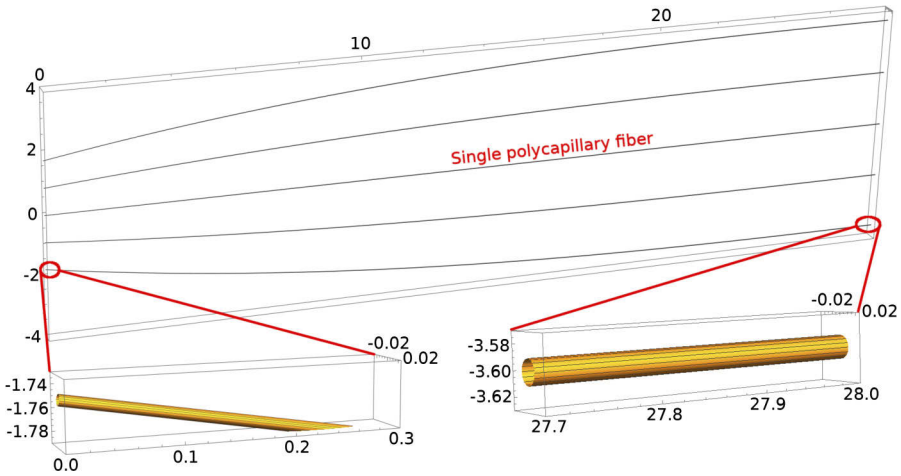


**Fig. 3.** (*Top*) Fiber shapes obtained using Eqs. (1), (2), and (4). The beginning (*Left bottom*) and the end (*Right bottom*) are shown enlarged in mm scale.

The total external reflection of X-ray can be described by the complex refractive index, which is defined as follows [26,27]:

$$n = 1 - \delta + i\beta, \tag{5}$$

where $1-\delta$ is the real part of the refractive index and $\beta$ is the imaginary part describing absorption of X-rays in the matter. The quantity $\delta$ is mostly in the order of $10^{-6}$ and the real part $1 - \delta$ is

Optics EXPRESS

smaller then 1, while $\beta$ is even less that $\delta$ [26]. In the X-ray region any medium, in particular solid, is optically less dense than air, which results in a refracted beam that is deflected toward the boundary plane. Consequently, there is the critical angle $\theta_{crit}$ for which no beam enters to the second medium ($\beta = 0$) and the boundary completely reflects the incident beam back into the first medium. According to Snell's law this critical angle of incidence is approximated by $\cos\theta_{crit} = n \approx 1 - \frac{\theta_{crit}^2}{2}$. The combination of this condition with Eq. (5) leads to the relation:

$$\theta_{crit} \approx \sqrt{2\delta} \sim 1/E, \tag{6}$$

where $E$ is the energy of X-ray photon.

The reflectivity, defined by the intensity ratio of the reflected beam and the incident beam, for X-rays hitting the smooth surface at incidence angle $\theta_i$ can be expressed by the Fresnel formula using the complex refraction index (Eq. (5)) in the following way [26]:

$$R_F(\theta_i) = \frac{(\theta_i - \theta_t')^2 + \theta_t''^2}{(\theta_i + \theta_t')^2 + \theta_t''^2}, \tag{7}$$

where $\theta_t'$ and $\theta_t''$ are real and imaginary components, respectively, of the refraction angle $\theta_t$. These formula is valid independent of the polarization of the incident beam because of the assumed small $\theta_i$ and $\theta_t$ angles [26]. The real and imaginary components of $\theta_t$ angle, can be written as follows:

$$\begin{aligned} \theta_t'^2 &= \tfrac{1}{2}\left(\sqrt{\left|(\theta_i{}^2 - 2\delta)^2 + 4\beta^2\right|} + (\theta_i{}^2 - 2\delta)\right), \\ \theta_t''^2 &= \tfrac{1}{2}\left(\sqrt{\left|(\theta_i{}^2 - 2\delta)^2 + 4\beta^2\right|} - (\theta_i{}^2 - 2\delta)\right). \end{aligned} \tag{8}$$

The real component $\theta_t'$ is decisive in the range above the critical angle, while the imaginary component $\theta_t''$ is dominant for angles below critical. Consequently, within this approach the reflection coefficient for a smooth surface can be expressed in terms of $\delta$ and $\beta$ parameters, which are available from CXRO base [54].

In fact, a real surface of glass is not ideally smooth and its quality is important factor for describing the transport properties of X-rays through the polycapillary. In the existing models describing the interactions of photons with rough surfaces, the well known approach is the exponential damping factor (EDF) [30]. According to the EDF model the modified $R_{EDF}$ X-ray reflectivity is described as follows:

$$R_{EDF}(\theta_i) = R_F(\theta_i) \cdot \exp\left(-\frac{(4\pi\sigma\sin\theta_i)^2}{\lambda^2}\right), \tag{9}$$

where $\sigma$ is the root-mean-square (rms) surface roughness parameter, and $\lambda$ is the wavelength of the incident X-ray. As it is noted in Ref. [30], the EDF model overestimates the roughness correction, because it describes only the specular reflection of the photons in the direction for which the incident and reflection angles are equal, and thus it neglects the dispersion of reflected X-rays around the specular direction. The other model taking into account also the diffuse scattering of X-rays at rough surfaces was described by Kimball *et al* [53] and an example of application of this model is presented in Ref. [30,40]. In this approach, the X-ray strikes on the surface at the angle $\theta_i$ smaller than critical $\theta_{crit}$ for the total external reflection. The reflected beam consists of a specular $R_S(\theta_i)$ component (assuming equality of incidence $\theta_i$ and reflection $\theta_r$ angles) and a diffuse $R_D(\theta_i)$ component (describing reflection at an angle different from the angle of incidence). The absolute reflectivity according to the Kimball approach, $R_K(\theta_i)$, is given

Optics EXPRESS

as the sum of specular $R_S(\theta_i)$ and diffuse $R_D(\theta_i)$ reflection coefficients:

$$R_K(\theta_i) = R_S(\theta_i) + R_D(\theta_i). \tag{10}$$

The specular component can be expressed by the modified Fresnel formula $R_S(\theta_i) = R_F(\theta_i) - \Delta R_S(\theta_i)$ (see Ref. [53]), where $R_F(\theta_i)$ is the Fresnel formula and $\Delta R_S(\theta_i)$ is the decrease coefficient. In this approach the scattering of photons from a rough surface at the small angles is characterized, by three dimensionless parameters:

$$\eta = \frac{\theta_i}{\theta_{crit}}, \qquad \tau = \frac{\sigma}{D}, \qquad \varphi = \frac{s}{P}, \tag{11}$$

where the $\eta$ is the ratio of the incident angle to the critical angle, the $\tau$ is the ratio of the rms $\sigma$ to the penetration depth $D$ (in normal direction to the surface) and $\varphi$ is the ratio of the roughness correlation length $s$ to the penetration path length $P = 2D/\theta_{crit}$ (in parallel direction to the surface). The decrease $\Delta R_S(\theta_i)$ of the Fresnel reflection coefficient is defined as:

$$\Delta R_S(\theta_i) = 4\eta\tau^2[\sqrt{r_A}\cos(\xi_A/2) - \sqrt{r_B}\sin(\xi_B/2)], \tag{12}$$

$$r_A = \sqrt{(1/\varphi)^2 + \eta^4}, \quad r_B = \sqrt{(1/\varphi)^2 + (1-\eta^2)^2},$$

$$\tan(\xi_A) = \frac{1}{\varphi\eta^2}, \quad \tan(\xi_B) = \frac{1}{\varphi(1-\eta^2)}.$$

The diffuse component $R_D(\theta_i)$ can be expressed by the differential form:

$$\frac{dR_D}{d\eta'} = \eta\eta'^2\tau^2\frac{8}{\pi}\left(\frac{\varphi}{1+\varphi^2(\eta^2-\eta'^2)^2}\right), \tag{13}$$

where $\eta' = \theta_{scat}/\theta_{crit}$ is characterized by the scattering angle $\theta_{scat}$. Integration of the Eq. (13) over $\eta'$ gives the probability of diffuse scattering by the rough surface.

The reflectivity of X-rays hitting the $SiO_2$ surface, calculated using Fresnel formula ($R_F$) (Eq. (7)) valid for the ideally smooth surface, EDF model ($R_{EDF}$) (Eq. (9)) and Kimball theory ($R_K$) (Eq. (10)), which includes corrections for the surface roughness, for 8.4 keV photon energy is shown in Fig. 4. The contributions of specular ($R_S$) and diffuse ($R_D$) reflectivity to the Kimball approach are also shown. For $\sigma = 0$ reflectivity curves for EDF and Kimball models coincide with the curve of Fresnel formula (ideal surface) ($R_F$). In that calculations the $\sigma$ and $s$ parameters were chosen respectively as 3 nm and 10 $\mu$m, which corresponds to typical values for $SiO_2$ [30]. It can be observed, that surface roughness significantly reduces the reflectivity. Additionally, the decrease of reflectivity in the EDF model is greater than the decrease in Kimball theory. Its caused by taking into account the diffuse scattering in Kimball model [53]. The diffuse scattering is described by correlation length $s$ expressing inequality in a direction parallel to the surface. The increase of correlation length reduces specular reflectivity with simultaneously growth of diffuse component. These models of reflectivity was used to simulate a transmission of X-rays through the $SiO_2$ polycapillary applied to collimate quasi-parallel photons beam from a small X-ray fluorescence emission spot.

### 2.2. Simulation of X-ray polycapillary optics properties

The simulation of polycapillary properties in focusing or collimating geometries are discussed in context of applications with the synchrotron radiation. In the simulations the X-ray transmission and focusing properties, such as focal distance, spot size and photon beam divergence were studied. The simulations were performed for the polycapillary made of $SiO_2$ (see Table 1), for

Optics EXPRESS

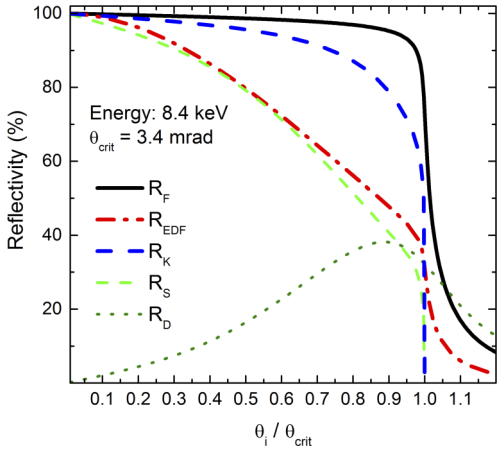


**Fig. 4.** Comparison of calculated reflectivity for X-ray of energy 8.4 keV reflected from $SiO_2$ material according to different models describing surface roughness: Fresnel formula ($R_F$), EDF model ($R_{EDF}$), Kimball theory ($R_K$) and its components: specular ($R_S$), and diffuse ($R_D$).

**Table 1. Summary of characteristics of the polycapillary installed in PBWDS spectrometer mounted at ESRF ID21 beamline. Data contained in the table are provided by the manufacturer XOS [55].**

| Polycapillary installed in PBWDS spectrometer | |
|---|---|
| Entrance: 3.5 mm | Focal distance: 10 mm |
| Exit: 7.2 mm | Capture angle: 20.04° |
| Length: 28 mm | Focus size: 50 – 100 $\mu$m |
| Transmission | Divergence |
| @1.5 keV: 33% | @8 keV: 3.4 mrad |
| @8 keV: 14% | |

X-ray energy range 1.45 keV – 8.5 keV. Based on the SEM photo [12], the single fiber diameter and wall thickness were assumed to be 10 $\mu$m and 1.5 $\mu$m, respectively.

A divergence of quasi-parallel photons beam formed by the polycapillary was studied with Monte-Carlo simulations using Kimball theory describing real surface. The Kimball theory was chosen because it includes both specular and diffuse reflectivity, and therefore contains the correct description of reflection of X-rays from the surface. The total divergence $\Delta\omega$ (double deviation of photons trajectory from symmetry axis of the polycapillary) was determined as a full width at the half of maximum of exit angle profile (Fig. 5). The simulated profiles of exit angle show that the total divergence strongly depends on the X-rays energy – decrease with increase of X-ray energy. These profiles show also the presence of a deep minimum intensity for an exit angle close to zero. This low intensity indicates a small number of photons passing through the polycapillary without reflection. The simulations of the divergence $\Delta\omega$ as a function of photons energy is shown in Fig. 6. For photon energy close to 10 keV, the exit angle is determined by the critical angle, that shows the good agreement between solid line (Eq. (6)) and simulated points. However, for small X-rays energy (about 2 keV) observed discrepancy between critical angle and simulated divergence is caused by geometrical limitations. As can be seen in Fig. 2(a), the fiber bending increases with increasing the entrance distance from the axis of the polycapillary,

Optics EXPRESS

that causing a growth of the entrance incident angle. For the fiber localized on the outer edge of the polycapillary, this angle, has a value of 9.3 mrad, which is smaller than critical angle for 2 keV photon energy. Therefore, for the X-ray energy about 2 keV, the beam divergence on polycapillary exit is determined by geometrical shape on polycapillary entrance.

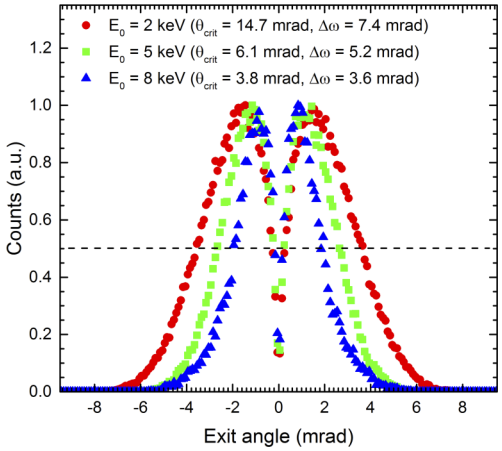


**Fig. 5.** Dependence of the total divergence $\Delta\omega$ of the X-ray beam outgoing the polycapillary for different photon energy, calculated with Monte-Carlo simulations.

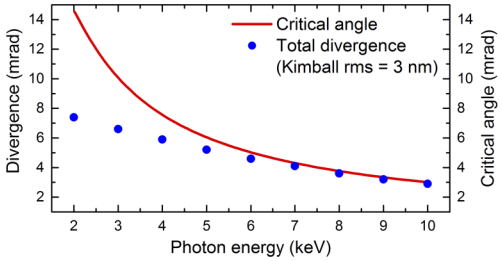


**Fig. 6.** Comparison of the theoretical critical angle with a Monte-Carlo simulations of total beam divergence for Kimball theory.

Simulated total divergence for X-rays with energy 8 keV is $\Delta\omega$ = 3.6 mrad, that corresponds with manufacturer data equal 3.4 mrad (see Table 1). The beam divergence is also visible in the Fig. 7 showing the simulated beam profiles for 8 keV X-rays at different distances (10 mm, 110 mm and 650 mm) behind the polycapillary. The middle picture on this figure clearly shows a structure containing local maxima on the X-rays intensity distribution. Similar structure was earlier observed [36,49,56] at the transition of photons by monocapillary. This structure is observed for distance in range of 50 mm – 190 mm behind the exit of polycapillary. For average distance between local maxima, equal 0.5 mm, this range corresponds to total beam divergence $\Delta\omega$ on the polycapillary exit. A number of observed maxima (on each slope) on the beam profile is equal to the most common number of X-ray reflections inside the polycapillary. This number, which is known from Monte-Carlo simulations, is six. The local maximum is generated by the group of photons with defined number of reflections. The group of X-rays with a higher number of reflection, exits the polycapillary with greater angle in respect to its axis. A higher number of reflections also means a lower probability of leaving the polycapillary, and lower intensity on the edges of the profile. Absence of structure in close distance behind the polycapillary (0 – 40 mm) is due to the fact that the group of photons with different number of reflection have not been yet

Optics EXPRESS

separated. With increasing the screen distance behind the polycapillary, the next maxima appear at the top and move down the slope. For distance of 250 mm behind polycapillary, the structure disappears, due to the divergence of each photon groups, and the slope becomes smooth. The cross-section through the photons beam, simulated for 650 mm behind polycapillary shows the intensity distribution on the surface of the spectrometer crystal.

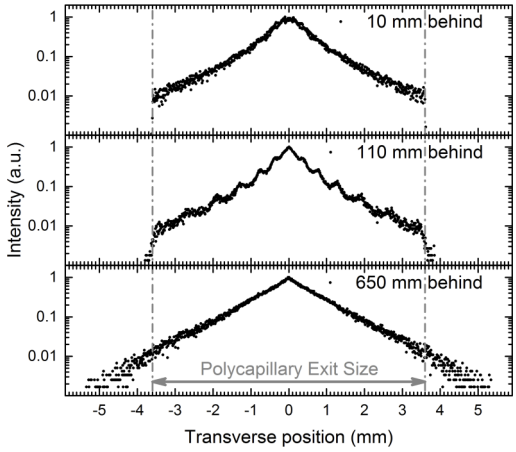


**Fig. 7.** Simulated intensity distribution for 8 keV X-rays along the central cross-section in distance of 10 mm *(top)*, 110 mm *(middle)* and 650 mm behind *(bottom)* the exit of polycapillary having an opening diameter of 7.2 mm.

The influence of the polycapillary shape on the basics properties such as transmission or divergence of beam of outgoing photons was also tested. The change of the shape of polycapillary was introduced by adding the distortion described by Gauss function, what enables the continuous adjustment of the effective curvature of the polycapillary. In this model, the Eq. (1) takes the form:

$$T(x,h) = \left(C_0(h) + C_1(h)x + C_2(h)x^2 + C_3(h)x^3\right) \cdot \left(1 + A \cdot \exp\left(-\frac{(x-\mu_G)^2}{2\sigma_G^2}\right)\right), \tag{14}$$

where $A$ is the magnitude of distortion, $\mu_G$ and $\sigma_G$ are the position and rms width of distortion, respectively. The distortion was applied in the middle part of polycapillary (10 mm$<\mu_G<$20 mm), and $\sigma_G = (5\% - 10\%)L$. Simulations have shown that the change of polycapillary shape over 5% of its diameter (which corresponds to approx. 15 fibers diameter) causes an almost 50% decrease in transmission. This result is consistent with the data of the paper describing the manufacturing process [50,51], which emphasizes that the profile of the polycapillary must be controlled with extremely small tolerance during production, to achieve the designed transmission, because any local distortions significantly worsen the properties of the polycapillary.

### 2.3. Simulations of X-ray track in the spectrometer

The simulation starts from generation of six random numbers, namely two photon emission angles $\xi$ and $\varphi$ in a spherical coordinate system, three coordinates $(x_s, y_s, z_s)$ of a point of photon emission and the photon energy $E$ taking into account a natural linewidth of the transition given by the Lorentz energy distribution. In terms of two angles $\xi$ and $\varphi$, a direction of the emitted photon in Cartesian coordinate system is determined. Each X-ray photon emitted by the source/sample is traced from the source to the polycapillary. The process of transition of X-rays through the polycapillary was described in details in Sec. 2.2. Parallel beam formed at the exit of

Optics EXPRESS

the polycapillary is directed on the flat crystal. The possible diffraction point of the photon at crystallographic plane $(x_k, y_k, z_k)$ is determined by solving an equation system of a straight line of photon path and crystal surface:

$$\begin{cases} x = x_p + P_X \cdot t, \\ y = y_p + P_Y \cdot t, \\ z = z_p + P_Z \cdot t, \\ \Upsilon x + \Phi y + \Psi z + \Omega = 0, \end{cases} \tag{15}$$

where the coordinate $(x_p, y_p, z_p)$ and $[P_X, P_Y, P_Z]$ represent the point and direction vector of photon on the exit of polycapillary respectively, the $\Upsilon$, $\Phi$ , $\Psi$ , $\Omega$ are the coefficients of the crystal plane in the coordinate system, and the photon trajectory is described parametrically by $t$. This system of equations describes an intersection point $(x_k, y_k, z_k)$ on a crystal surface. For each calculated diffraction point $(x_k, y_k, z_k)$, the angle $\theta$ between photon direction and crystallographic plane is calculated. The difference $\Delta\theta_{RCV} = \theta - \theta_B$ , where $\theta_B$ is the Bragg angle, determines the probability of X-ray diffraction according to the dynamical theory [5,6,57] described by the diffraction profile called crystal rocking curve, obtained from XOP2.3 [29] using XCRYSTAL module which is dedicated to flat perfect and mosaic crystals. The Bragg angle $\theta_B$ binding the crystallographic structure of a crystal with the wavelength of incident photons as described by Bragg's law [16]:

$$m\lambda = 2d_{hkl} \sin\theta_B, \tag{16}$$

where $m$ denotes the order of diffraction, $\lambda$ is the X-ray wavelength, and $d_{hkl}$ is the spacing constant of the diffraction planes $(hkl)$. The photon diffracted from the crystal with a direction $\overrightarrow{K} = [K_X, K_Y, K_Z]$ is traced on its way to the X-ray detector. The point $(x_d, y_d, z_d)$ of recording of the photon is calculated by solving the system of equations describing the intersection of a straight line diffracted photon path and a plane representing the detector surface.

In a typical simulation $N_{rand} = 10^8$ photons were randomly generated to obtain of about $N = 2.5 \cdot 10^4$ photons hitting the X-ray detector. For practical reasons the photons were generated in a cone with opening angle 15° covering only a small fraction of the full solid angle which was safe and efficient solution allowing to speed up the simulations. For these conditions, the typical statistical uncertainties of the maxima of simulated energy profiles ($\sqrt{N}/N$) were in the range of 3% – 5%, allowing thus to estimate the FWHM energy resolution of these profiles at the level of accuracy of less than 3%, and transmission at the level of accuracy of 5%. The computing time needed to simulate this number of events was about 60 min for a standard personal computer, where most of the time required for the computation was consumed by calculating the transmission process through the polycapillary.

The Monte-Carlo simulations of X-ray-tracing in the spectrometer allowed for the determination of the polycapillary transmission as well as the spectrometer energy resolution.

## 3. Experiment description

The results of simulations were next compared with the experiment data. The experiment was carried out at the European Synchrotron Radiation Facility (ESRF). The PBWDS spectrometer is integrated with the Scanning X-ray Microscope (SXM) chamber on the ID21 beamline (see Fig. 8). At this beamline the photons beam was produced by an undulator and monochromatized by a double-crystal Si(111) monochromator, which gives the energy resolution of $\Delta E/E = 10^{-4}$. The photons beam passed to SXM was focused to the spot size of order $1 \times 1$ $\mu$m$^2$ and photon flux of $10^9$ – $10^{10}$ per second. The sample was placed at an angle of 60° to the synchrotron X-ray beam.

Optics EXPRESS

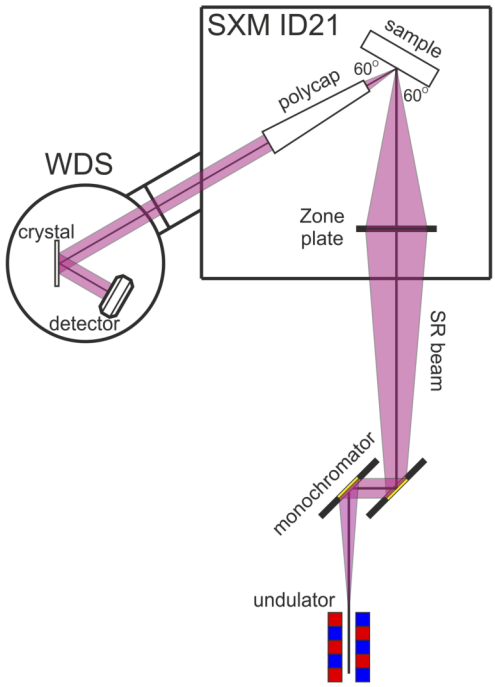


**Fig. 8.** Scheme of the measurement system on ID21 beam line with installed PBWDS spectrometer.

The polycapillary was installed at the angle of 60° to the sample surface and at the distance of about 10 mm from the sample. The $\theta$-$2\theta$ stage is mounted independently within the distances polycapillary-crystal and crystal-detector about 65 cm and 7 cm, respectively. The spectrometer is equipped with different flat crystals: ADP(101), Si(111), Ge(220) or LiF(220). All crystals were 60 mm wide (meridional plane) and 40 mm high (sagittal plane). The spectrometer can work in Bragg angle range of 20°-70°. The X-rays were detected by a gas-flow proportional counter with 12 $\mu$m thickness Be window and diameter of 22 mm. This detector is filled with P10 gas mixture (10% methane and 90% argon) with a flow rate of about 25 s.c.c.m (standard cubic centimeters per minute) at the atmospheric pressure and the thickness of the gas layer inside is 38 mm. Each fluorescence spectrum was recorded by scanning the desired angular range. The exposure time was 1 s per point/step, the number of measured points depended on the sample and was between 200 and 400 which corresponds to energy steps of 1 eV or 2 eV. Each measurement was preceded by reading current beam photon flux and optimizing the polycapillary focal position on the sample.

The experimental transmission $T_{cap}(E_i)$ was determined from recorded fluorescence lines. The number of photons registered by detector is connected with the photon flux by formula:

$$I(E_0, E_i) = I_0 F_{smp}(E_0, E_i) \left(\frac{\Omega}{4\pi}\right) T_{cap}(E_i) R_{eff}(E_i) \varepsilon_{det}(E_i), \tag{17}$$

where $I_0$ is the intensity of primary beam on the sample, $F_{smp}(E_0, E_i)$ is coefficient of intensity of X-ray fluorescence, $\Omega/4\pi$ is the capture angle of polycapillary with transmission $T_{cap}(E_i)$, $R_{eff}(E_i)$ is the effective reflectivity of the crystal and $\varepsilon_{det}(E_i)$ is the detector efficiency.

The coefficient of fluorescence intensity of X-rays with energy $E_i$ excited in the sample having the thickness $d_{smp}$ by the primary beam $E_0$ incident on the sample at an angle $\theta_{in}$ and observed at

Optics EXPRESS

an angle $\theta_{out}$ is expressed by:

$$F_{smp}(E_0, E_i) = Q \int_0^{d_{smp}} e^{-\frac{\mu^{tot}(E_0)\rho}{\sin\theta_{in}}x} \cdot \frac{\mu^{ph}(E_0)}{\sin\theta_{in}} \cdot e^{-\frac{\mu^{tot}(E_i)\rho}{\sin\theta_{out}}x} dx, \tag{18}$$

where $\mu^{tot}(E_0)$, $\mu^{tot}(E_i)$ are total mass absorption coefficients of primary and fluorescence photons respectively, $\mu^{ph}(E_0)$ is photoelectric mass absorption coefficient of primary beam and $\rho$ is the sample density. The excitation factor $Q = Jf\omega$ is expressed as the product of transition probability $f$, fluorescence yield $\omega$ and the absorption jump ratio $J = \frac{r-1}{r}$, where $r$ is jump factor. These factors are taken from XRAYLIB data table [58]. The effective crystal reflectivity $R_{eff}(E_i)$ is the probability that the photons with density distribution $\omega(\theta)$ incident on the crystal characterized by rocking curve $R(\theta)$ will be diffracted.

The effective crystal reflectivity can be expressed by formula $R_{eff}(E_i) = \int d\theta R(\theta)\omega(\theta)$, where $\int d\theta R(\theta) = R_{int}(E_i)$ is the integrated reflectivity of crystal [59]. The values of the crystal effective reflectivity $R_{eff}(E_i)$ used to determine the experimental value of polycapillary transmission $T_{cap}(E_i)$ can be obtained from computer simulations. Using the Monte-Carlo method the effective reflectivity can be expressed as the ratio of the number of X-rays diffracted from the crystal $N_{diff}$ to the X-rays departing from polycapillary $N_{dep}$, that is $R_{eff}(E_i) = \frac{N_{diff}}{N_{dep}}$. The uncertainty of the measured X-ray transmission results mainly from crystal perfection (quality). Based on available data, this uncertainty can be estimated at the level of 30%–40% [60], which has a decisive influence on the measured X-ray transmission value through the polycapillary.

The efficiency of gas detector $\varepsilon_{det}(E_i)$ was calculated taking into account the transmission through a detector window $T_w$, absorption $A_{det}$ in the gas and probability of X-ray escape $P_{esc}$ from the detector and can be expressed as $\varepsilon_{det} = T_w A_{det}(1 - P_{esc})$ [61].

## 4. Comparison of simulations with measurements

As a first application, series of X-ray fluorescence spectra of $K\alpha$, $K\beta$ and $L\alpha$, $L\beta$ lines for several elements from Al to Sn were measured. In the Fig. 9, as examples, the X-ray fluorescence spectra of Al, Sc and Mn are shown. These spectra were measured for ADP(101), Si(111) and Ge(220) crystals and for three energies of the synchrotron beam $E_0$ (4.1 keV, 4.5 keV, 7.15 keV), respectively. All of these crystals provide good resolution of the spectrometer and separation of $K\alpha$ and $K\beta$ emission lines. In the case of Al a small peak on the higher-energy side of the $K\alpha$ fluorescence corresponds to $L$-line satellite [62]. The experimental X-ray lines were compared with the simulated curves and good agreement was observed.

In order to show an influence of the polycapillary on the measured X-ray lines, simulations of X-ray profile of Mn $K\alpha$ line for PBWDS spectrometer in configuration with and without a polycapillary optics were performed. The results, shown in Fig. 10, clearly indicate a significant advantage of using of polycapillary for collimating the quasi-parallel X-ray beam. Application of polycapillary optics causes both the hundredfold increase of the peak intensity as well as a significant improvement of spectrometer energy resolution.

The Fig. 11 shows the simulated energy resolution compared with experimental data for ADP(101), Si(111) and Ge(220) crystals for different beam energies. The uncertainty value of experimental energy resolution of the PBWDS spectrometer was estimated at the level of 10%. The diffraction profile for silicon and germanium crystals were calculated with XOP software, while for ADP crystal it was generated using Gaussian distribution with parameters reported by Feldman [63]. The results of the Monte-Carlo simulation are in good agreement with experimental data. For ADP(101) crystal the resolution between 4 eV and 27 eV was achieved for photon energy in range between 1.45 keV and 3 keV. The results obtained for Si(111) crystal are between 5 eV and 25 eV for photon energy in the range between 2.5 keV and 4.5 keV. For

Optics EXPRESS

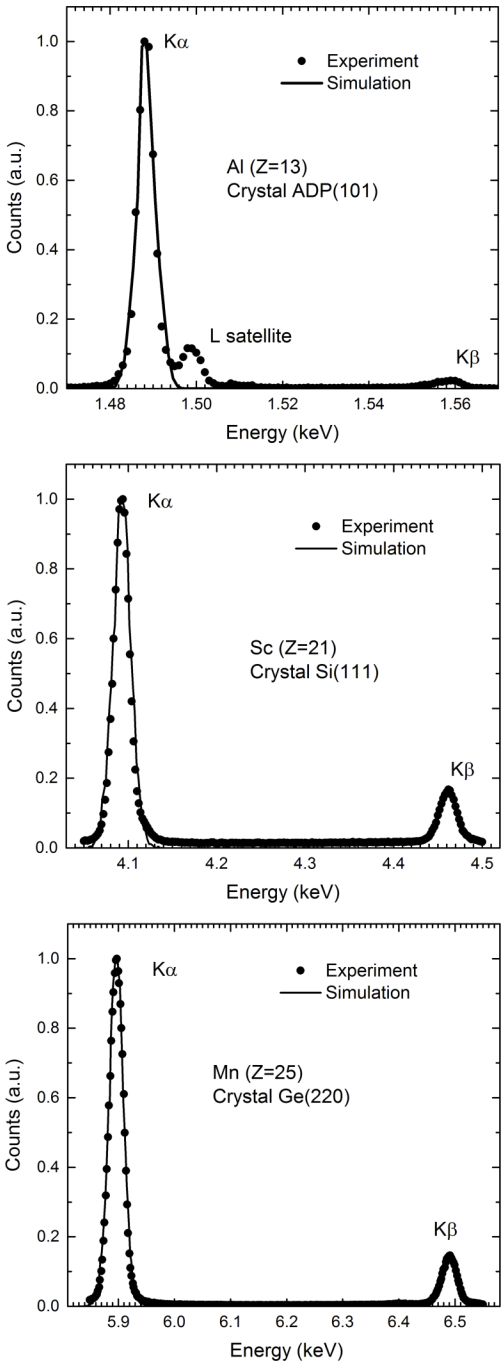


**Fig. 9.** Examples of X-ray fluorescence lines of Al $K\alpha, \beta$, Sc $K\alpha, \beta$ and Mn $K\alpha, \beta$ lines measured for ADP(101), Si(111) and Ge(220) crystals, respectively, registered by PBWDS spectrometer (points) and obtained in Monte-Carlo simulations (solid lines).

Optics EXPRESS

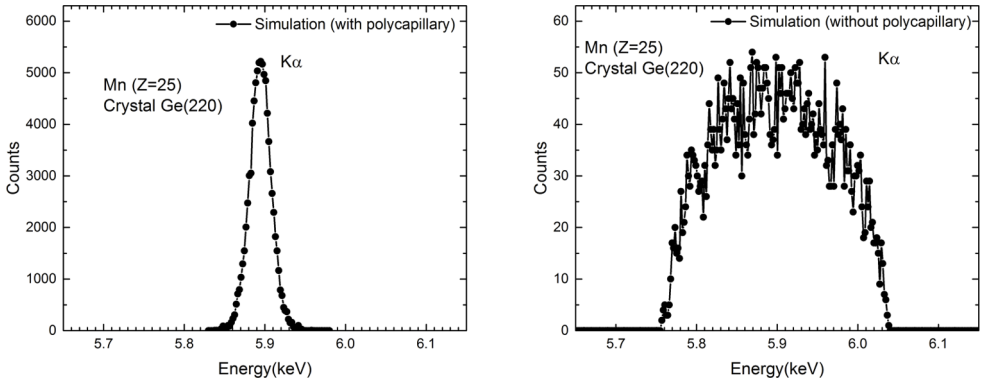


**Fig. 10.** Simulated X-ray profile of Mn $K\alpha$ line obtained for Ge(220) crystal and the configuration with (*Left*) and without (*Right*) a polycapillary optics.

Ge(220) crystal results are between 6 eV and 32 eV for photon energy range 3.5 keV – 6.5 keV. As can be seen in Fig. 11, the energy resolution of PBWDS spectrometer with germanium crystal is about two times better than the energy resolution measured with silicon crystal. Similarly, the energy resolution of the spectrometer with silicon crystal is about two times better than the energy resolution with ADP crystal. The experiment also confirmed the simulations, that the energy resolution of the PBWDS spectrometer with flat crystal and polycapillary, is a linear function of photon energy.

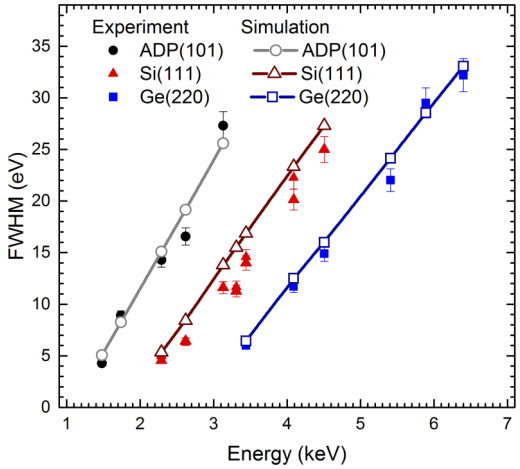


**Fig. 11.** Comparison of the measured energy resolution of the spectrometer and the Monte-Carlo simulations for Si(111), Ge(220) and ADP(101) crystals. Results of the simulations (open symbols) are connected with solid lines to guide the eye.

The influence of angular divergence of the X-ray beam ($\Delta\theta$) on the energy resolution ($\Delta E$) can be derived from the Bragg law (Eq. (16)) by calculating the derivative of $E$ as a function of the Bragg angle $\theta_B$, which leads to:

$$\Delta E = E \cdot \Delta\theta \cdot \cot\theta_B. \tag{19}$$

In case of PBWDS spectrometer the divergence of the beam ($\Delta\theta$) is expressed by the convolution of beam divergence on the polycapillary exit ($\Delta\omega$) and crystal rocking curve ($\Delta\theta_{RCV}$). However the crystal response (~100 $\mu$rad) is an order of magnitude smaller than the divergence of the

Optics EXPRESS

beam at the exit of polycapillary (~mrad, see Fig. 5) and its contribution is very small. As follows from the computer simulation, the beam divergence is the inverse function of photon energy ($\Delta\theta \sim \frac{\text{const}}{E}$) (see Fig. 6), and from the Bragg law (Eq. (16)) the sine of Bragg angle is also the inverse function of photon energy ($\sin\theta_B \sim \frac{\text{const}}{E}$), therefore the expression on the energy resolution can take the form $\Delta E \sim E\cos\theta_B$. For the X-ray energy for which the angle $\theta_B$ is small, the energy resolution linearly depends on the photon energy. When the photon energy is accordingly small (large Bragg angle $\theta_B$), the factor $\cos\theta_B$ plays an important role and the energy resolution is no longer linear. Numerical calculations show that the factor $\cos\theta_B$ is significant for the energy corresponding to the Bragg angle greater than 65 degrees. This Bragg angle range was not used in this study.

The Fig. 12 shows the comparison of transmission of the polycapillary, measured (points) and calculated (lines), with respect to discussed in Sec. 2.2 theories, for X-ray energies in the range of 1.5 keV – 8.0 keV. The theoretical value of the transmission with a perfectly smooth surface of fibers presents the curve described by Fresnel formula [26]($T_F$). The transmission calculated after taking into account inequality of the surface of fibers, is illustrated by curves described by EDF [30] ($T_{EDF}$) and Kimball [53] ($T_K$) models, respectively. A significant decrease of transmission efficiency at around 1.9 keV, is caused by the absorption edge of silicon, the component of the polycapillary glass material.

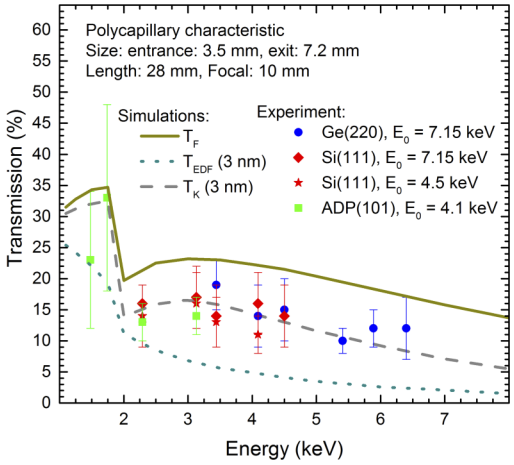


**Fig. 12.** Comparison of measured and simulated transmission of polycapillary installed on PBWDS spectrometer as a function of incident photon energy. Theoretical predictions were calculated for smooth ($T_F$) and rough surface calculated according to the EDF model ($T_{EDF}$) and Kimball theory ($T_K$) for surface roughness rms = 3 nm. Experimental points were obtained from recorded fluorescence spectra.

From the comparison of the experimental data of transmission with the simulations, it may be noted that qualitative changes in transmission are properly described by Fresnel ($T_F$) and Kimball ($T_K$) models. The transmission calculated using Kimball model best describes the experimental values of transmission. On the other hand, the EDF model does not describe correctly the transmission, because it does not take into account a diffusion reflectivity on polycapillary surface. Additionally, the dependence of X-ray transmission through the polycapillary as a function of photons energy, obtained in the Monte-Carlo simulation, is consistent with the simulation results presented at the work [41].

As the example of the spectrometer application, the spectra of few mineral samples were measured at the synchrotron micro-spectroscopy ID21 beamline at ESRF. In the Fig. 13 the spectrum of Monazite mineral ((La,Ce,Nd,Gd)$PO_4$) measured with PBWDS spectrometer

Optics EXPRESS

equipped with Ge(220) crystal for primary photon energy of 7.15 keV is shown. Measurements of mineral samples have shown that it is possible to separate the fluorescent lines of lanthanide *L*-series, which is a typical problem in X-ray fluorescence analysis.

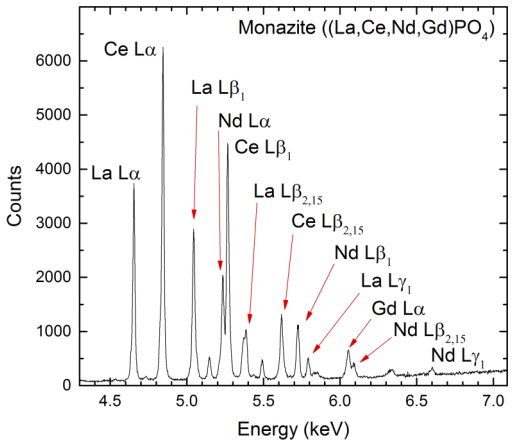


**Fig. 13.** Fluorescence spectrum of Monazite ((La,Ce,Nd,Gd)$PO_4$) measured with PBWDS spectrometer equipped with germanium (220) crystal.

## 5. Conclusions

The proposed Monte-Carlo simulations program, allows for a tracing of X-rays passing through the polycapillary optics, as well as for the optimization of the parallel-beam wavelength-dispersive (PBWDS) spectrometer. The X-ray-tracing program provides the information on transmission efficiency, divergence of the beam outgoing the polycapillary for different photons energy, and X-rays intensity distribution behind the polycapillary. This program allows also to calculate the efficiency and energy resolution of the PBWDS spectrometer designed for X-rays energy range of 1.45 keV – 8.5 keV. The predictions of the X-ray-tracing Monte-Carlo simulations, concerning the instrumental polycapillary transmission and energy resolution of the spectrometer, were compared with the results of experimental studies at ID21 beamline at the ESRF (Grenoble), showing good agreement. Slight differences are due to the unknown deviations of the polycapillary shape compared to the assumed one.

**Disclosures.** The authors declare no conflicts of interest.

**Data availability.** Data underlying the results presented in this paper are not publicly available at this time but may be obtained from the authors upon reasonable request.

## References

1. E. Tsompopoulou and K. Mergia, "Energy dispersive x-ray fluorescence spectroscopy and applications in material science," HNPS Proc. **21**, 145–147 (2019).
2. M. J. Pushie, I. Pickering, M. Korbas, M. Hackett, and G. George, "Elemental and chemically specific x-ray fluorescence imaging of biological systems," Chem. Rev. **114**(17), 8499–8541 (2014).
3. J. Börjesson and S. Mattsson, "Medical applications of x-ray fluorescence for trace element research," Powder Diffr. **22**(2), 130–137 (2007).
4. M. Cotte, J. Szlachetko, S. Lahlil, M. Salomé, V. A. Solé, I. Biron, and J. Susini, "Coupling a wavelength dispersive spectrometer with a synchrotron-based X-ray microscope: A winning combination for micro-X-ray fluorescence and micro-XANES analyses of complex artistic materials," J. Anal. At. Spectrom. **26**(5), 1051–1059 (2011).
5. W. H. Zachariasen, Theory of X-ray diffraction in crystals (Dover Publications, New York, 1967).
6. B. E. Warren, *X-ray diffraction* (Dover Publications Inc., New York, 1969).
7. J. Als-Nielsen and D. McMorrow, *Elements of Modern X-ray Physics* (John Wiley & Sons, England, 2nd edition, 2011).

Optics EXPRESS


8. M. A. Kumakhov, "Channeling of photon and new X-ray optics," Nucl. Instrum. Methods Phys. Res., Sect. B **48**(1-4), 283–286 (1990).
9. M. A. Kumakhov, "Capillary optics and their use in X-ray analysis," X-Ray Spectrom. **29**(5), 343–348 (2000).
10. S. Dabagov, S. Nikitina, M. Kumakhov, N. Ibraimov, G. Vartaniants, A. Nikitin, and L. Spielberger, "Focusing of X-rays by capillary systems," Nucl. Instrum. Methods Phys. Res., Sect. B **103**(1), 99–105 (1995).
11. S. Dabagov, A. Marcelli, G. Cappuccio, and E. Burattini, "On propagation of x-rays in capillary channels," Nucl. Instrum. Methods Phys. Res., Sect. B **187**(2), 169–177 (2002).
12. P. J. Schields, D. M. Gibson, W. M. Gibson, N. Gao, H. Huang, and I. Y. Ponomarev, "Overview of polycapillary X-ray optics," Powder Diffr. **17**(2), 70–80 (2002).
13. J. Szlachetko, M. Cotte, J. Morse, M. Salomé, P. Jagodziński, J.-C. Dousse, J. Hoszowska, Y. Kayser, and J. Susini, "Wavelength-dispersive spectrometer for X-ray microfluorescence analysis at the X-ray microscopy beamline ID21 (ESRF)," J. Synchrotron Rad. **17**(3), 400–408 (2010).
14. S. Lahlil, M. Cotte, I. Biron, J. Szlachetko, N. Menguy, and J. Susini, "Synthesizing lead antimonate in ancient and modern opaque glass," J. Anal. At. Spectrom. **26**(5), 1040–1050 (2011).
15. J. Hoszowska, J.-C. Dousse, J. Szlachetko, Y. Kayser, W. Cao, P. Jagodziński, M. Kavčič, and S. H. Nowak, "First observation of Two-Electron One-Photon transitions in single-photon K-shell double ionization," Phys. Rev. Lett. **107**(5), 053001 (2011).
16. W. H. Bragg and W. L. Bragg, "The reflection of X-rays by crystals," Proc. R. Soc. Lond. A **88**(605), 428–438 (1913).
17. B. R. Maddox, M. C. Akin, A. Teruya, D. Hunt, D. Hahn, J. Cradick, and D. V. Morgan, "Single-pulse x-ray diffraction using polycapillary optics for in situ dynamic diffraction," Rev. Sci. Instrum. **87**(8), 083901 (2016).
18. C. A. MacDonald and W. M. Gibson, "Applications and advances in polycapillary optics," X-Ray Spectrom. **32**(3), 258–268 (2003).
19. C. A. MacDonald, "Focusing polycapillary optics and their applications," X-Ray Opt. Instrum. **2010**, 1–17 (2010).
20. C. A. MacDonald and J. C. Petruccelli, "Polycapillary optics for medical applications," J. Phys.: Conf. Ser. **776**, 012001 (2016).
21. H. Yan, X. Ma, W. Sun, S. Mendez, S. Stryker, S. Starr-Baier, G. Delliturri, D. Zhu, R. Nath, Z. Chen, K. Roberts, C. MacDonald, and W. Liu, "Monte Carlo dosimetry modeling of focused kV x-ray radiotherapy of eye diseases with potential nanoparticle dose enhancement," Med. Phys. **45**(10), 4720–4733 (2018).
22. S. Dabagov and Y. Gladkikh, "Advanced channeling technologies for x-ray applications," Radiat. Phys. Chem. **154**, 3–16 (2019).
23. P. Jagodziński, M. Pajek, D. Banaś, H. Beyer, M. Trassinelli, and T. Stöhlker, "Ray-tracing simulations of spherical Johann diffraction spectrometer for in-beam X-ray experiments," Nucl. Instrum. Methods Phys. Res., Sect. A **753**, 121–130 (2014).
24. P. Jagodziński, J. Szlachetko, J.-C. Dousse, J. Hoszowska, M. Szlachetko, U. Vogelsang, D. Banaś, T. Pakendorf, A. Meents, J. A. van Bokhoven, A. Kubala-Kukuś, M. Pajek, and M. Nachtegaal, "A DuMond-type crystal spectrometer for synchrotron-based X-ray emission studies in the energy range of 15-26 keV," Rev. Sci. Instrum. **90**(6), 063106 (2019).
25. M. Matsumoto and T. Nishimura, "Mersenne Twister: A 623-dimensionally equidistributed uniform pseudo-random number generator," ACM Trans. Model. Comput. Simul. **8**(1), 3–30 (1998).
26. R. Klockenkämper, *Total-Reflection X-ray Fluorescence Analysis* (Wiley, New York, 1997).
27. D. Attwood, *Soft X-rays and Extreme Ultraviolet Radiation: Principles and Applications* (Cambridge University Press, New York, 1999).
28. M. S. del Río, C. Ferrero, and V. Mocella, "Computer simulation of bent perfect crystal diffraction profiles," Proc. SPIE **3151**, 312–323 (1997).
29. M. S. del Río, "Ray tracing simulations for crystal optics," Proc. SPIE **3448**, 230–245 (1998).
30. L. Vincze, K. Janssens, F. Adams, A. Rindby, and P. Engström, "Interpretation of capillary generated spatial and angular distributions of X-rays: Theoretical modeling and experimental verification using the European Synchrotron Radiation Facility optical beam line," Rev. Sci. Instrum. **69**(10), 3494–3503 (1998).
31. B. Chen, "A new algorithm for x-ray transmission through a cylinder capillary," Nucl. Instrum. Methods Phys. Res., Sect. B **170**(1-2), 230–234 (2000).
32. B. Chen, "Theoretical consideration of x-ray transmission through cylinder capillaries," Rev. Sci. Instrum. **72**(2), 1350–1353 (2001).
33. S. Peng, Z. Liu, T. Sun, K. Wang, L. Yi, K. Yang, M. Chen, and J. Wang, "Simulation of transmitted x-rays in a polycapillary x-ray lens," Nucl. Instrum. Methods Phys. Res., Sect. A **795**, 186–191 (2015).
34. L. Yu-De, L. Xiao-Yan, L. Shi-Gang, H. Jin-Long, G. Fei, S. Tian-Xi, and L. Peng, "Polycapillary X-ray lens for the secondary focusing Beijing synchrotron radiation source," Chin. Phys. B **22**(4), 044103 (2013).
35. A. Liu, "The x-ray distribution after a focussing polycapillary - a shadow simulation," Nucl. Instrum. Methods Phys. Res., Sect. B **243**(1), 223–226 (2006).
36. L. Vincze, K. Janssens, F. Adams, and A. Rindby, "Detailed ray-tracing code for capillary optics," X-Ray Spectrom. **24**(1), 27–37 (1995).
37. G.-J. Chen, F. Cerrina, K. F. Voss, K. H. Kim, and F. C. Brown, "Ray-tracing of X-ray focusing capillaries," Nucl. Instrum. Methods Phys. Res., Sect. A **347**(1-3), 407–411 (1994).

Optics EXPRESS


38. K. Furuta, Y. Nakayama, M. Shoji, R. Kaigawa, K. Hanamoto, H. Nakano, and Y. Hosokawa, "Theoretical consideration of intensity of an X-ray microbeam formed by a hollow glass pipe," Rev. Sci. Instrum. **64**(1), 135–142 (1993).
39. X. Lin, A. Liu, Y. Li, and P. Wu, "A MATLAB programming for simulation of X-ray capillaries," App. Maths. Comp. **172**(1), 188–197 (2006).
40. L. Wang, B. K. Rath, W. M. Gibson, J. C. Kimball, and C. A. MacDonald, "Performance study of polycapillary optics for hard x-rays," J. Appl. Phys. **80**(7), 3628–3638 (1996).
41. P. Tack, T. Schoonjans, S. Bauters, and L. Vincze, "An X-ray ray tracing simulation code for mono- and polycapillaries: Description, advances and application," Spectrochim. Acta, Part B **173**, 105974 (2020).
42. X. Wang, Y. Li, M. Zhou, J. Duan, H. Luo, L. Ye, X. Liu, and X. Lin, "Theoretical simulation of X-ray transmission through a polycapillary X-ray lens with a variable capillary radius," IEEE Trans. Nucl. Sci. **67**(5), 791–796 (2020).
43. L. Vincze, S. V. Kukhlevsky, and K. Janssens, "Simulation of poly-capillary lenses for coherent and partially coherent x-rays," Proc. SPIE **5536**, 81–85 (2004).
44. Z. Chi, "GXPS: A Geant4-based Monte-Carlo code for x-ray polycapillary simulation," J. Appl. Phys. **128**(12), 124902 (2020).
45. A. Liu, "Simulation of x-ray beam collimation by polycapillaries," Nucl. Instrum. Methods Phys. Res., Sect. B **234**(4), 555–562 (2005).
46. A. Liu and Y. Lin, "Simulation of x-ray transmission in capillaries with different profiles," Math. Comput. Sim. **66**(6), 577–584 (2004).
47. F. C. Brown, K. H. Kim, S. M. Heald, B. M. Barg, and E. A. Stern, "Use of the program SHADOW in designing a capillary-focusing beamline," Rev. Sci. Instrum. **67**(9), 3379–3380 (1996).
48. D. Hampai, S. B. Dabagov, G. Cappuccio, and G. Cibin, "X-ray propagation through polycapillary optics studied through a ray tracing approach," Spectrochim. Acta, Part B **62**(6-7), 608–614 (2007).
49. D. Hampai, S. B. Dabagov, G. Cappuccio, and G. Cibin, "X-ray propagation through hollow channel: PolyCAD – a ray tracing code," Nucl. Instrum. Methods Phys. Res., Sect. B **244**(2), 481–488 (2006).
50. N. Gao and I. Y. Ponomarev, "Polycapillary x-ray optics: manufacturing status, characterization and the future of the technology," X-Ray Spectrom. **32**(3), 186–194 (2003).
51. D. H. Bilderback, "Review of capillary x-ray optics from the 2nd International Capillary Optics Meeting," X-Ray Spectrom. **32**(3), 195–207 (2003).
52. A. Bjeoumikhov, N. Langhoff, R. Wedell, V. Beloglazov, N. Lebed'ev, and N. Skibina, "New generation of polycapillary lenses: manufacture and applications," X-Ray Spectrom. **32**(3), 172–178 (2003).
53. J. C. Kimball and D. Bittel, "Surface roughness and the scattering of glancing-angle X-rays: Application to X-ray lenses," J. Appl. Phys. **74**(2), 877–883 (1993).
54. "CXRO: The Center for X-ray Optics," http://cxro.lbl.gov (accessed March, 2021).
55. "XOS," http://www.xos.com (accessed March, 2021).
56. E. Denisov, V. Glebov, and N. Zhevago, "Focusing of x-rays using tapered waveguides," Nucl. Instrum. Methods Phys. Res., Sect. A **308**(1-2), 400–404 (1991).
57. A. H. Compton and S. K. Allison, *X-rays in Theory and Experimentn* (Van Nostrand, New York, 1935).
58. M. S. del Río, A. Brunetti, B. Golosio, A. Somogyi, and A. Simionovici, "XRAYLIB tables (X-ray fluorescence cross-section)," http://ftp.esrf.eu/pub/scisoft/xraylib/xraylib_tables_v2.3.pdf (accessed March, 2021).
59. J. Härtwig, "On the integrated reflectivity of perfect crystals in extremely asymmetric bragg cases of x-ray diffraction," Acta Crystallogr., Sect. A: Cryst. Phys., Diffr., Theor. Gen. Crystallogr. **37**(6), 802–804 (1981).
60. B. L. Henke, E. M. Gullikson, and J. C. Davis, "X-ray interactions: Photoabsorption, Scattering, Transmisson, and Reflection at E=50-30000 eV, Z=1-92," At. Data Nucl. Data Tables **54**(2), 181–342 (1993).
61. M. Pajek, A. P. Kobzev, R. Sandrik, R. A. Ilkhamov, and S. H. Khusmurodov, "Accurate efficiency determination of a Si(Li) detector in the Si-K and Au-M absorption edge energy region," Nucl. Instrum. Methods Phys. Res., Sect. B **42**(3), 346–358 (1989).
62. O. Mauron, J.-C. Dousse, J. Hoszowska, J. P. Marques, F. Parente, and M. Polasik, "*L*-shell shake processes resulting from 1s photoionization in elements $11 \leqslant Z \leqslant 17$," Phys. Rev. A **62**(6), 062508 (2000).
63. U. Feldman, G. A. Doschek, and R. W. Kreplin, "High-resolution X-ray spectra of the 1979 march 25 Solar flare," Astrophys. J. **238**, 365–374 (1980).